RSC Advances

ROYAL SOCIETY OF CHEMISTRY

www.rsc.org/advances

RSC Advances

RSCPublishing

ARTICLE

Copper Atoms Embedded in Hexagonal Boron Nitride as Potential Catalysts for CO Oxidation: A First-principles Investigation

Cite this: DOI: 10.1039/x0xx00000x

Received 00th January 2014,
Accepted 00th January 2014

DOI: 10.1039/x0xx00000x

www.rsc.org/

Xin Liu,[a]* Ting Duan,[a] Yanhui Sui,[a] Changgong Meng,[a] and Yu Han[b]

We addressed the electronic structure of Cu atoms embedded in hexagonal boron nitride (*h*-BN) and their catalytic role in CO oxidation by first-principles-based calculations. We showed that Cu atoms prefer to bind directly with the localized defects on *h*-BN, which act as strong trapping sites for Cu atoms and inhibit their clustering. The strong binding of Cu atoms at boron vacancy also up-shifts the energy level of Cu-d states to the Fermi level and promote the formation of peroxide-like intermediate. CO oxidation over Cu atoms embedded in *h*-BN would proceed through the Langmuir–Hinshelwood mechanism with the formation of a peroxide-like complex by reaction of coadsorbed CO and O_2, with the dissociation of which the a CO_2 molecule and an adsorbed O atom are formed. Then, the embedded Cu atom is regenerated by the reaction of another gaseous CO with the remnant O atom. The calculated energy barriers for the formation and dissociation of peroxide complex and regeneration of embedded Cu atoms are as low as 0.26, 0.11 and 0.03 eV, respectively, indicating the potential high catalytic performance of Cu atoms embedded in *h*-BN for low temperature CO oxidation.

Introduction

Recent theoretical and experimental results demonstrated that sub-nanometer transition metal (TM) nanoparticles (NPs) or even single TM atoms can exhibit superior catalytic activity and selectivity than conventional nano-sized particles in a large number of important chemical reactions.[1-5] For example, although bulk gold has long been thought to be catalytically inactive, free[6-11] and especially metal oxide supported Au clusters of about 2 nm in size exhibit rather high catalytic activity for CO oxidation.[12-19] The underlying enhancing mechanisms are not always straightforward. Unlike NPs of sp metals, where the impact of quantum size effect would be significant due to free-electron like behavior of s and p electrons,[20] the reactivity of TM NPs are determined by their localized d states.[21] Therefore, low-coordination and unsaturated atoms often function as reaction sites over TM NPs [22] and downsizing the particles to single atoms is highly desirable to maintain a high density of active sites for catalytic reactions.[23] On the other hand, the support–metal interaction in deposited TM NPs is also of great importance. This interaction would raise strains, shift the energy levels, redistribute electron density of the NP states and thus change the catalytic activity of the nanocatalysts. Careful selection of the support allows the electronic states in the TM NPs to be finely tuned, making the TM NPs highly reactive or completely inert.[24-28] This may also help to effectively stabilize the tiny TM NPs or atoms and prohibit them from sintering under realistic reaction conditions, which are the key challenges for fabrication of practical and stable single-atom catalysts.[29, 30] To this end, a careful screening of the metal-support interactions would be necessary to rationalize the design of monodispersed ultrafine TM NPs or single TM atoms as efficient catalyst for a specific reaction.

Many studies on supported metal clusters show that surface defects of the supports could serve as anchoring sites for metal clusters or even single atoms. Mono-dispersed Pt, Ir and Au atoms deposited on defects of TM oxides have been proved to be efficient catalysts for a series oxidative reactions including CO oxidation.[4, 5, 31] Apart from the oxides, various defects, including boundaries, dopants, vacancies and etc in graphene have also been proposed to modulate the electronic structures and so as the catalytic performance of supported TM NPs.[32-39] More recently, single atom doped graphene was fabricated by electron-beam radiation.[40] Au, Cu, Fe and Pt atoms embedded in graphene have been predicted to be efficient for CO catalytic oxidation theoretically. The promoted catalytic activity can be attributed to the partially occupied d states localized in the

[a] *School of Chemistry, Dalian University of Technology, Dalian, China; E-mail: xliu@dlut.edu.cn.* [b] *Advanced Membranes and Porous Materials Center, Physical Sciences and Engineering Division, King Abdullah University of Science and Technology, Thuwal 23955-6900, Saudi Arabia.*

vicinity of the Fermi level (E_F) due to the interaction of the TM atom with graphene.[41-45] These investigations provide strong evidence that fabrication of mono-dispersed TM atom catalyst by introduction of defects onto the support is a feasible method and the resulting catalyst can display unusual behaviors compared with conventional catalysts.

The fabrication and utilization of hexagonal boron nitride nanosheet, which has similar planar structure like graphene but with different chemical and physical properties, has drawn considerable attention in recent years.[46-51] Different from the conjugated π bonding among C atoms in graphene, the B-N interaction in *h*-BN is more ionic and the potential interaction and charge transfer with the deposited TM atoms maybe quite different. Unlike graphene, *h*-BN are stable under high temperatures up to 1000 K. There are also various defects, such as vacancies, exist in the synthesized *h*-BN sheets.[52] These defects could be created in a controllable way by electron beam irradiation.[53] With the help of high-resolution transmission electron microscopy, the atomic structure of the defects structures in *h*-BN have been solved. Boron monovacancies are found to be preferably formed, and the dominating zigzag-type edges are proven to be N terminated which is accord with the theoretical prediction.[54, 55] The facile synthesis of defective *h*-BN provides a new platform for fabrication of finely dispersed TM catalysts. [56] Recently, Co, Ru, Fe and Au atoms embedded in *h*-BN were proposed to be effective for CO oxidation, however the role of interfacial interaction to catalytic performance has been seldom explored.[56-59]

In this work, we investigated the electronic structure of Cu atoms embedded in *h*-BN and the mechanisms of CO catalytic oxidation to CO_2 on them by first-principles-based calculations. We focused the impact of the strong interaction between Cu atoms and the defect states on *h*-BN on the stability, electronic structure and potential catalytic performance of the embedded Cu atoms. The possible reaction mechanisms for CO oxidation were studied and compared, based on the calculated thermodynamics and kinetics data. These findings pave the way for the development of effective CO oxidation catalysts with high stability and superior catalytic performance.

Theoretical Methods

The first-principles based calculations were carried out using the DMol^3 package.[60, 61] Perdew-Burke-Ernzerhof (PBE) functional within the formulation of gradient approximation (GGA) was used to handle the exchange and correlations.[62] The ion-electron interaction is described with DFT semicore pseudopotentials (DSPPs) and a double numerical basis set including a d-polarization function (DND).[63] Within this scheme, the B, C, N and O atoms were treated with all-electron basis-sets, while the core Cu electrons were described by DSPP pseudopotential and the valence Cu electrons were handled with DND basis-sets. All self-consistent field calculations were performed with a convergence criterion of 2×10^{-4} eV on the total energy. To lower the computational cost in geometry optimization, the substrate and the embedded composites were preoptimized with empirical potential,[64, 65] and then were fully relaxed within the aforementioned ab-initio scheme until the residue forces were reduced below 1×10^{-2} eV/Å. To ensure high-quality results, the real-space global orbital cutoff was chosen as 4.6 Å. With the above setup, the bulk lattice parameter of face-center-cubic Cu is reproduced as a =3.66 Å, while the B-N distance in pristine *h*-BN is 1.46 Å.[66, 67]

A hexagonal 6 × 6 supercell containing 36 BN units was used to mimic the *h*-BN and the doped composite (Cu-BN). Embedding of Cu atom was done by substituting one B/N atom with a Cu atom. The minimum distance between the *h*-BN sheet and its mirror images was set to be larger than 20 Å to avoid the interactions among them. Brillouin zone integration was sampled over a Γ centered 4 × 4 × 1 *k*-point grid in geometric optimization and the search for the transition state (TS), while a 20 × 20 × 1 Monkhorst-Pack *k*-point grid was used to explore the electronic structures.[68] Test calculations using a 162-atom supercell (9 × 9 *h*-BN supercell) gave essentially the same results. The amount of charge transfer was investigated within the Hirshfeld scheme.[69]

The transition states (TSs) were located by the synchronous method with conjugated gradient refinements.[70] This method involves linear synchronous transit (LST) maximization, followed by repeated conjugated gradient (CG) minimizations, and then quadratic synchronous transit (QST) maximizations and repeated CG minimizations until a TS is located. These TSs were further confirmed by the frequency analysis.

The binding energy (E_b) of Cu atom onto *h*-BN was calculated as the energy difference between the Cu atomically deposited *h*-BN (CuBN) and the separated *h*-BN plus the freestanding Cu atom, following Equation (1).

$$E_b = E_{CuBN} - (E_{Cu} + E_{BN}) \quad (1)$$

The formation energy (E_f) of a structure was calculated with respect to the stoichiometry (n_x) and the chemical potential (μ_x, x=B, N or Cu) of each elements that was taken from gaseous N_2, metallic α-B and face-center-cubic Cu, following Equation (2).

$$E_f = E_{total} - \sum_x n_x \mu_x \quad (2)$$

For the study concerning adsorption of CO, O_2, O and etc., the adsorption energy (E_{ad}) was calculated as the energy difference between the species absorbed Cu deposited *h*-BN and the gaseous species plus the bare CuBN, following Equation (3).

$$E_{ad} = E_{adsorbate+CuBN} - (E_{CuBN} + E_{adsorbate}) \quad (3)$$

Results and discussion

Cu atomic deposition on *h*-BN

The optimized structures, binding energies for the Cu atoms deposited on pristine *h*-BN and embedded in defective *h*-BN are summarized in Table 1. According to the symmetry of *h*-BN lattice, there are 4 possible deposition structures (Fig. 1), namely the AtopN site that is on top of an N atom, the AtopB site which is on top of a B atom, the BrgBN site that is in the middle of the B-N bridge and the Hol site that is on top of the center of the hexagonal B_3N_3 ring.

Table 1. Optimized structures and energetics for Cu atomic deposition on *h*-BN.

Model	E_b[a] (eV)	h[b] (Å)	Min R_{Cu-B}[c] (Å)	Min R_{Cu-N}[d] (Å)	Δq[e] (e)
Pristine *h*-BN					
AtopN	-0.22	2.18	2.66	2.18	0.13
AtopB	-0.14	2.34	2.34	2.80	0.11
BrgBN[f]					
Hol	-0.08	2.40	2.82	2.82	0.10
Defective *h*-BN					
CuBSV	-6.07	1.53	2.79	1.83	0.43
CuNSV	-2.66	1.74	2.14	3.02	0.18

[a] The binding energy of Cu atom onto pristine and defective *h*-BN, calculated from Equation 1. [b] The distance of Cu atom from the basal plane of *h*-BN. [c] The minimum distance from the deposited Cu atom to B atom on *h*-BN. [d] The minimum distance from the deposited Cu atom to N atom on *h*-BN. [e] The amount of charge transfer from Cu atom to the *h*-BN. [f] Diffuses to AtopN.

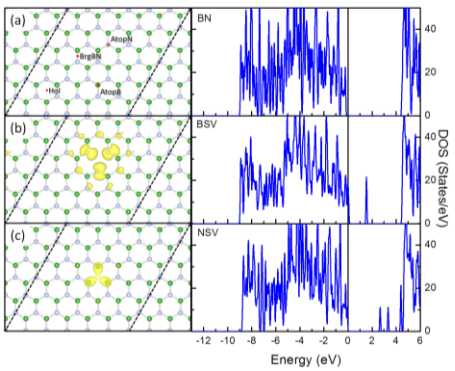

Fig. 1 Optimized structures of *h*-BN, BSV, NSV (left panel) and their density of states (DOS, right panel). (B: Green; N: Light blue. The contour value of the charge density of defect states are both 0.005 a.u. The blue line in the right panel corresponds to the sp-DOS of B and N atoms. The DOS curves are aligned by the calculated valence band maximum.)

Among these 4 structures, the Cu atomic deposition at AtopN was found most stable while AtopB ranks the second. In the AtopN structure, Cu atom stands 2.18 Å above a surface N atom and the nearest B–Cu distance is 2.66 Å. The calculated E_b at AtopN is -0.22 eV. As for the AtopB structure, the distance from Cu atom to the basal *h*-BN plane is 2.34 Å, while the nearest Cu-N distance is 2.80 Å. As a result from the large separation between the Cu atom and *h*-BN surface, the AtopB is 0.08 eV less stable than AtopN. The BrgBN structure was found unstable and would evolve to AtopN structure during the structural optimization. In the Hol structure, the Cu atom locates 2.40 Å above the center of the B_3N_3 hexagon ring and the nearest B–Cu and N-Cu distances are all about 2.82 Å. The calculated E_b for Hol site is only -0.08 eV and is 0.14 eV less stable as compared with AtopN. It should be noted that the estimated amount charge transfer upon deposition is only about 0.10 |*e*| from the Cu atom to *h*-BN sheet. Furthermore, the magnetic moment of the whole system, which is localized on the Cu atom, is the same as the magnetic moment of free Cu atom. All these suggest the weak interaction formed between the Cu atom and *h*-BN sheet and is accord with the small E_b for Cu deposition over pristine *h*-BN.

One of the key challenges in fabrication of practical and stable single-atom catalysts is that, single atoms are too mobile and easy to sinter under realistic reaction conditions.[29, 30] The calculated barrier for Cu atoms diffusion along the AtopN to the nearest neighboring AtopB on pristine *h*-BN is as low as 0.08 eV and is in reasonable agreement with the barrier for Ru and Fe atomic diffusion on *h*-BN.[57, 58, 71] This implies that the deposited Cu atoms are ready to diffuse on pristine *h*-BN and will form large particles as the amount of deposited Cu atoms increases. As a result, pristine *h*-BN is not eligible as a support material to stabilize the Cu atoms for catalytic applications. Many studies on supported metal catalysts show that defects of the support materials could serve as anchoring sites for metal clusters and even single atoms.[19, 25, 72, 73] Recent investigations on synthesized *h*-BN shows that there are many defects, including vacancies, exist in the synthesized *h*-BN sheets.[52] The atomic structures of the defects in *h*-BN have been solved by high-resolution transmission electron microscopy. Boron monovacancies are found to be plausible and the N terminated zigzag-type edges are identified to be dominating which is accord with the theoretical prediction.[54, 55, 74] Therefore, monovacancies were considered as the typical defects on *h*-BN.

Removal of one B atom forms a boron single vacancy (BSV, Fig. 1), while removal of one N atom forms a nitrogen single vacancy (NSV, Fig. 1) on *h*-BN. After removal of the B/N atom, the charge density over the atoms around the vacancy will reorganize to minimize the instability caused by the generation of the vacancy. The atoms around the defect were deformed from their original position. In the optimized structures, the N-N distances among the 3 N atoms in BSV are elongated from 2.52 Å in pristine *h*-BN to 2.68 Å and the B-N-B angle around the defect is distorted from 120° in pristine *h*-BN to 126°. With the same mechanism, the B-B distances among the B atoms in NSV are shortened from 2.52 Å in pristine *h*-BN to 2.32 Å and the N-B-N angle is deformed to 115.41°. The difference in atomic distortion when a B or N vacancy is generated can be understood with the localized charge on it. When a B atom is removed, 3 B-N bonds are broken and the negatively charged dangling bonds will localize on N atoms and make them repulsive to each other. When a NSV is generated, the edge B atoms are less charged as compared in pristine *h*-BN, so the repulsive interactions among them are decreased.

The DOS of BSV, NSV and *h*-BN are compared in Fig. 1 to highlight the impact of vacancy formation on the reactivity of the BN support. Instead of presenting a wide gap of 4.23 eV in pristine *h*-BN, the formation of BSV and NSV introduces sharp spikes into the bulk band gap of *h*-BN (Fig. 1). These states were further proved to be contributed mainly by the N/B atoms adjacent to the vacant position by DOS analysis. The wavefunctions of these defect states were also extracted in left panel of Fig. 1, confirming their localized nature. According to the DOS curves, both BSV and NSV will exhibit higher reactivity to the deposited TM atoms as compared with *h*-BN. In this sense, the edge atoms (B or N) with localized defect states can be expected to act as anchoring points to stabilized single TM atoms.

Due to the larger size of Cu atoms as compared with B or N atoms, when a Cu atom is placed above a vacancy, it moves outward the basal plane of *h*-BN after geometry optimization. The outwards movements of Cu atoms are 1.53 Å and 1.74 Å for BSV and NSV, respectively. Compared with the case of Cu atomic deposition on pristine *h*-BN, the charge on Cu atom at the BSV (CuBSV) doesn't change significantly, which indicates a less ionic nature of the interaction between the Cu atom and the N atoms around the vacancy. The differential charge density showed that there are significant red charge accumulation regions between the Cu atoms and the N atoms, implying that the partially covalent nature of the interaction (Fig. 2). The E_b at BSV (-6.07 eV) is thus enhanced by more than twenty folds as compared with that on pristine *h*-BN.[56] The large E_b of CuBSV also makes the outward diffusion of Cu to its neighboring Hol site endothermic by 5.85 eV. The computed diffusion barrier is 6.65 eV and is much higher than the diffusion barrier of 0.08 eV on pristine *h*-BN, which vigorously excludes the clustering problem on CuBSV. The deposition of Cu atom on NSV (CuNSV) was also investigated and the corresponding E_b is -2.66 eV, which is 3.41 eV less stable as compared with CuBSV.

To strengthen the above discussion on the relative stability among these defective structures, the E_f of each structure was calculated with respect to the composition of the structure and chemical potential of each elements following eq(2). The E_f of pristine *h*-BN is -62.75 eV and that for BSV is -54.84 eV, implying that formation of BSV requires an energy input of about 8 eV. As for the Cu embedded structures, the E_fs are -56.45 eV and -54.53 eV for CuBSV and CuNSV, respectively, which further supports the superior stability of CuBSV as compared with CuNSV. It should also be noted that, though higher than that of *h*-BN, the E_f of CuBSV is still 1.61 eV lower than that of BSV proving that the formation of CuBSV is ready to take place in existence of Cu atoms and BSV. As the recent theoretical and experimental investigations already showed that BSV is more stable than NSV and is most likely the defect structures formed, we will focus on CuBSV in the followed discussion.[54, 55, 74]

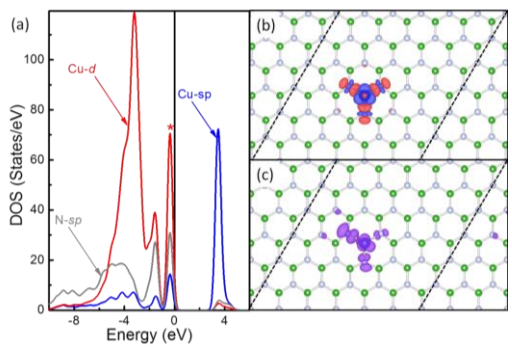

Fig. 2 DOS (a), contour plots of differential charge density (b) and electron density of the Cu-N interaction state right below the E_F(c) of CuBSV. (B: Green; N: Light blue. The contour value of the differential charge density and electron density are both ± 0.005 a.u. The charge accumulation regions are in red and the charge depletion regions are in blue. The DOS curves are aligned by the calculated E_F.)

To gain deeper insight into the significantly enhanced E_b in CuBSV, the projected density of states (PDOS) of the Cu-sp, Cu-d and N-sp states of Cu and N atoms at BSV is plotted in Fig. 2. The DOS of *h*-BN with a vacancy is characterized with sharp peaks inside the bulk band gap, which is obviously different from the case of pristine *h*-BN (Fig. 1). After Cu deposition, the peaks at the E_F and the sharp spikes in the band gap of N-sp states are shifted downwards and overlap with the Cu-sp and Cu-d states below E_F, showing the strong hybridization among these states. This, together with the differential charge density, suggest that the Cu atom uses its valence states to interact with the defective states of the BSV. The electron densities of the hybridized state right below with the E_F (marked with red *) were extracted in Fig. 2, showing the localized nature of the interaction among Cu-d, Cu-sp and N-sp states of N atoms around the vacancy. Due to these interaction, some states of the Cu-d states are upshifted to E_F and resonance strongly with N-sp states. The energy levels of localized d states of transition metals are known to be vital for the activation of adsorbed reactants and subsequent reaction. Previously, Cu is known to be less active for CO oxidation due to its low and filled d-states.[21] This upshift of Cu-d states, originated from the Cu-N interaction, suggest that CuBSV may exhibit higher reactivity in activation of adsorbed CO and O_2 for CO oxidation.

O_2, CO, O and CO_2 adsorption on CuBSV

The stability of reactants, intermediates, transition states and products would strongly affect the thermodynamics of a specific reaction. For the CO oxidation over CuBSV, the possible reactants and products are O_2, CO, O and CO_2. The adsorption of these species were investigated by first-principles-based calculations and the most plausible adsorption structures and corresponding E_{ad}s are summarized in Table 2 and Fig. 3. We noticed that both CO_2 and O_2 are only physisorbed on the pristine *h*-BN. The adsorption stabilities of CO and O_2 are significantly enhanced on CuBSV, with the E_{ad}s change from less than -0.10 eV to -1.05 and -0.75 eV, respectively, indicating that both of them can be readily adsorbed onto the CuBSV at moderate temperatures.

Table 2. The E_{ad}s and the most plausible structures of various reaction species adsorption on CuBSV.

Species	E_{ad}[a] (eV)	Bonding Details	
		Bond	Length (Å)
CO	-1.05	C-O	1.16
		Cu-C	1.87
O_2	-0.75	O-O	1.33
		Cu-O	2.03
		Cu-O	2.03
CO_2	-0.01	Cu-O	2.65
		C-O	1.17
		C-O	1.18
O	-2.54	Cu-O	1.75

[a.] The E_{ad} is calculated as the energy difference between the species adsorbed on CuBSV and the gaseous species plus the bare CuBSV according to equation 3.

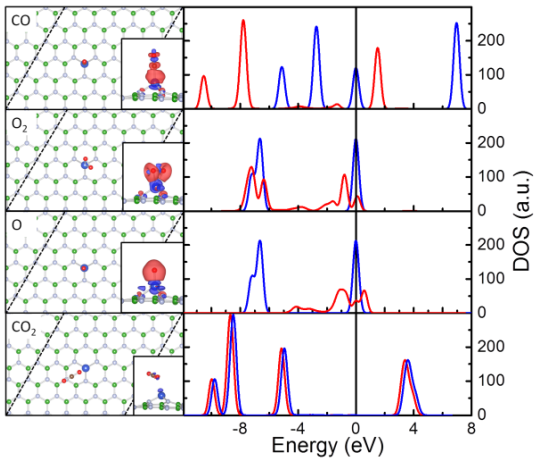

Fig. 3 The most plausible adsorption structures (left panel), contour plots of differential charge density (insets of left panel) and the corresponding DOS curves (right panel) for CO, O_2, O and CO_2 adsorption on CuBSV. (B: Green; N: Light blue; Cu: Deep blue; O: Red. For the contour plots, the charge accumulation regions are rendered in red while the charge deplete regions are shown in blue. The contour value of the differential charge density and electron density are both ± 0.005 a.u. The DOS curves of free species are in blue and those of absorbed species are in red. The DOS curves are aligned by the calculated E_F.)

CO interacts strongly with the CuBSV. The calculated E_{ad} for the most plausible adsorption configuration is -1.05 eV, which is even stronger than the E_{ad} of CO over bulk Cu surfaces.[75] In this configuration, CO interacts with the Cu atom by standing nearly vertically to the basal plane of *h*-BN right on top of the embedded Cu atom. The C-Cu distance is 1.87 Å, which falls in the range of typical C-Cu chemical bonding. The covalent nature of this interaction is supported by the large charge accumulation region between the C and Cu atoms. There is a charge transfer of 0.02 |*e*| from the CuBSV to the CO, which is the net result of the donation of CO-5σ electrons to Cu states and the back-donation of Cu-d electrons into the CO-2π* states. This charge transfer activates the CO molecule and this activation is visualized by the charge accumulation region between C and Cu atoms and the charge depletion region between the C and O atoms in the contour plot of differential charge density. Originated from this charge transfer, the C-O distance is elongated from 1.14 Å in a free molecule to 1.16 Å after adsorption. Due to the interaction with the CuBSV, all the DOS peaks corresponding to CO states are downshifted and the peak of 2π* orbital is split into parts and even shifted to below E_F.

The E_{ad} of O_2 molecule is about 0.3 eV less stable as compared with that of CO and the adsorption configuration is quite different. The O_2 molecule prefers to lie parallel to the basal plane of the *h*-BN, immediately on top of the embedded Cu atom. The 2 nearest Cu-O distances are 2.03 and 2.02 Å, respectively. The amount of charge transfer from CuBSV to the absorbed O_2 is 0.24 |*e*|. This charge transfer is confirmed by the charge depletion region on the embedded Cu atom and the charge accumulation region on O_2 molecule. The DOS peaks of O_2-5σ and O_2-2π states are downshifted as compared with those of the freestanding O_2 and coincide in energy range with those of Cu-d and Cu-sp states (Figs. 2 and 3), showing the strong hybridization among them. Furthermore, due to the charge transfer from Cu-d state to the O_2-2π, both the energy level and intensity of O_2-2π state are changed significantly. The elongation of the O-O distance by about 0.2 Å and the charge depletion region between the 2 O atoms vigorously visualize this activation. It should be noticed that the calculated E_{ad} of CO and O_2 are larger as compared with those reported by Lin et al., this can be understood by the small (3×3) *h*-BN slab model used by Lin et al and the different implementation of the density functional theory in DMol3 and VASP, where only interactions among valence electrons are considered in VASP, while C and O are treated with full electron basis sets to include interaction among non-valence electrons within CO molecule and Cu-d states in DMol3.[56]

We also investigated the O atomic adsorption on CuBSV. As compared with the case of O_2, the E_{ad} of O atom is enhanced by about 1.80 eV to -2.54 eV. Similar to the case of O_2 adsorption, the absorbed O atom gains charge from CuBSV and the amount of charge transfer is 0.34 |*e*|. The interaction between Cu and O is mainly ionic as visualized by the differential charge density analysis. In this sense, the enhancement of O E_{ad} can be understood as the result of removing of repulsive interaction among negative charged absorbed O atoms as compared with the case of O_2. This phenomenon is widely observed in coverage dependent O adsorption on surfaces of transition metals and alloys.[76, 77] In the DOS plots, the peaks of O-sp states overlap with those of Cu-sp and Cu-d states around the E_F, showing the strong hybridization among them. The large intensity of the O-sp states at the E_F also suggests the potential high oxidation activity of the absorbed O atom. The shape and energy levels of O-sp states of adsorbed O atom are quite similar to those of adsorbed O_2, indicating the effectiveness of CuBSV for O_2 activation.

Various possible adsorption sites for CO_2 molecule were investigated and the most stable adsorption site locates on the Cu atom with an E_{ad} of -0.01 eV. In this configuration, the O-Cu distance is 2.65 Å and one of the C=O is pointing to the embedded Cu with a C-O-Cu angle of 122.27°. According to the DOS plots, the peaks of CO_2 states are only downshifted slightly and no significant change of the shape and intensity of these peaks can be observed. The contour plot of the differential charge density shows that this weak CO_2 adsorption can be understand as the formation of an electrostatic Lewis acid-base adduct, where the embedded Cu that is charge deficient and acts as the Lewis acid, while the partially negatively charged O end of CO_2 acts as the Lewis base. This kind of CO_2 adsorption mechanism is widely used in development of off-framework charge centers in activated mesoporous carbon for CO_2 capture and sequestration. [78]

It should be noted that from an energetic point of view, the adsorption of CO on CuBSV is preferred rather than the O_2 molecule. The coadsorption of CO and O_2 on the same embedded Cu atom is also an exothermic process and the E_{ad} is -0.91 eV and is even larger than the separate adsorption of O_2 (-0.75 eV). Previously, Kim et al showed that H_2 can take over

the absorbed CO at elevated H_2 pressure even though CO binds strongly on subnanosized Pt particles deposited on graphene.[79] Considering the CO catalytic oxidation normally happens in O_2-rich environment, the large free energy change during the reaction will drive the CO oxidation to proceed over CuBSV even though it has a slightly larger affinity to CO.

CO oxidation over CuBSV

In general, CO oxidation can take place through 2 mechanisms, namely the Langmuir-Hinshelwood (LH) and the Eley- Rideal (ER) mechanism, depending on the catalysts involved.[80] The ER mechanism initiates with the direct reaction of gaseous CO molecules with the adsorbed O atom at the reaction centers, resulting from the activation of O_2. Considering the high activity of adsorbed O atom, the activation of O_2 is the rate limiting step. Different from the ER mechanism, the CO oxidation following LH mechanism starts with the interaction between the coadsorbed CO and O_2 molecules for formation of a peroxide-like O=C-O-O intermediate. As the coadsorbed CO and O_2 are all negatively charged and repulsive to each other, the formation of the peroxide becomes harder and sets the rate of the whole process. The reaction of CO with O_2 over CuBSV through both the ER and LH mechanisms was investigated.

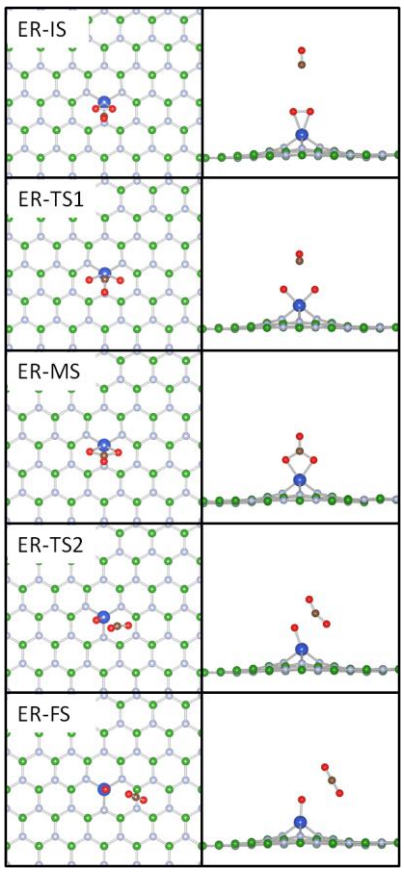

Fig. 4 Top views (left panel) and side views (right panel) of local configurations of the adsorbates on the CuBSV at various states along the minimum-energy pathway via the ER mechanism, including the initial state (ER-IS), transition state (ER-TS1 and ER-TS2), intermediate state (ER-MS) and final state (ER-FS). (B: Green; N: Light blue; Cu: Deep blue; O: Red; C: Brown.)

To search for the minimum-energy path (MEP) for the CO oxidation, the state of gaseous CO and O_2 and clean CuBSV was set as the energy zero and the configuration of physisorbed CO above preadsorbed O_2 on CuBSV was selected as the initial state (ER-IS). The atomic configurations at various states along the reaction path following the ER mechanism were shown in Fig. 4. When one CO molecule approaches the activated O_2, CO is inserted into the O-O bond to form a carbonate-like intermediate state (ER-MS) on CuBSV, where the O-O distance is further elongated to 2.19 Å as compared with the case for O_2 adsorption. Similar elongation of the O-O distance has been observed in the reaction of CO with O_2 over Fe-embedded graphene and supported Au nanoparticles.[9, 13, 43] This CO insertion is exothermic by 3.57 eV and the corresponding reaction barrier is 1.91 eV (ER-TS1) due to the breaking of the O-O bond and the formation of the new C-O bonds. Then, this reaction MEP connects ER-MS with the residual intermediate state (ER-FS) where the carbonate-like structure in ER-MS dissociates by scission of one of C-O bond attaching to the Cu atom. This will form a physisorbed CO_2 and an O atom adsorbed on the CuBSV (ER-FS). As the ER-MS is relatively stable and the adsorbed single O atom is highly reactive, the reaction along this path is endothermic by 1.15 eV with respect to ER-MS and requires crossing of another high energy barrier of 1.38 eV (ER-TS2). Considering the E_{ad}s of both CO and O_2 are both lower than the reaction barrier of the formation of ER-MS, desorption of adsorbed CO and O_2, rather than formation of ER-MS, would take place if there is no alternative MEPs for the CO oxidation to take place. This indicates that CO oxidation over CuBSV via the ER mechanism is almost impossible or proceeds with great difficulty thermodynamically. This conclusion is further enhanced when we consider the more favorable E_{ad} of CO on CuBSV. This finding is different from the cases of CO oxidation over Fe, Ru and Co atoms embedded in *h*-BN where the ER mechanism is considered to be dominant due to the strong affinity of these TM atoms to O_2. Previously, Lu et al., Song et al. and Gao et al investigated the CO oxidation over Au and Cu atoms embedded in graphene and *h*-BN, they all proposed that LH mechanism is more favorable in energy than the ER mechanism for the CO oxidation to take place.[41, 44, 59] Therefore, we emphasized on the LH mechanism.

Table 3. Structural Parameters for Various States along the MEP for the CO Oxidation over CuBSV through LH mechanism.

States	$d_{C\text{-}O}$[a] (Å)	$d_{C\text{-}Cu}$[a] (Å)	$d_{C\text{-}O1}$[a] (Å)	$d_{O1\text{-}O2}$[a] (Å)	$d_{O2\text{-}Cu}$[a] (Å)	$\angle_{O\text{-}C\text{-}O1}$[b] (°)
LH-IS1	1.15	2.09	2.64	1.28	2.16	113.9
LH-TS1	1.17	2.02	1.79	1.34	2.09	116.5
LH-MS	1.21	2.01	1.34	1.49	1.96	124.9
LH-TS2	1.21	2.10	1.29	1.68	1.89	130.4
LH-FS1	1.18	2.89	1.18	3.18	1.75	177.0

[a] The distance between specific atoms. Please see Fig. 5 for the nomination of atoms. [b] The angle among O-C-O1. This angle is 120° in CO_3^{2-} and is 180° in CO_2.

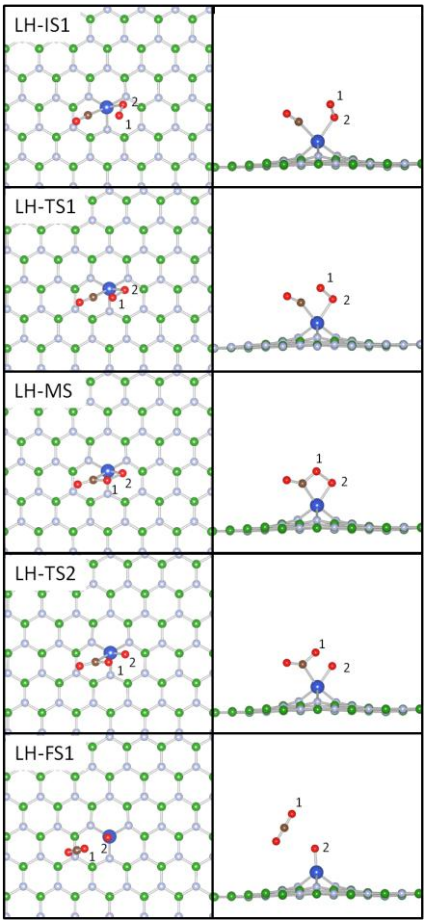

Fig. 5 Top views (left panel) and side views (right panel) of local configurations of the adsorbates on the CuBSV at various states along the minimum-energy pathway via the LH mechanism, including the initial state (LH-IS1), transition state (LH-TS1 and LH-TS2), intermediate state (LH-MS) and final state (LH-FS1). (B: Green; N: Light blue; Cu: Deep blue; O: Red; C: Brown.)

According to the LH mechanism, the coadsorbed CO and O_2 (LH-IS1) will react to form a peroxide-like intermediate (LH-MS) and then with the scission of the O-O bond in LH-MS, a physisorbed CO_2 is formed together with an adsorbed atomic O on the CuBSV (LH-FS1). Following this, another gaseous CO molecule will approach to and react with the adsorbed atomic O (LH-IS2) and form a second physisorbed CO_2 (LH-FS2). Finally, the catalytic cycle restarts after the desorption of the CO_2 with the coadsorption of O_2 and CO.

The most plausible coadsorption structures of CO and O_2, together with the atomic structures at various states along the MEP following the LH mechanism are shown in Fig. 5 and Fig. 6, with the structural parameters listed in Table 3 and Table 4.

Once CO and O_2 are coadsorbed onto the CuBSV (LH-IS1), one of the O atom (O1) in the adsorbed O_2 molecule starts to approach the carbon atom of CO to reach the transition state (LH-TS1) that connects LH-IS1 to LH-MS on the MEP. During this endothermic process, the O-O distance in O_2 is elongated from 1.27 Å in LH-IS1 to 1.34 Å in LH-TS1. Accompanying this, the C-O1 distance also decreases from 2.09 Å in LH-IS1 to 2.01 Å in LH-TS1. The energy barrier for the formation of LH-MS is 0.26 eV and a peroxide-like O2-O1-C-O complex is thus formed. In LH-MS, the O-O distance is further elongated to 1.49 Å. The O-O distance of this length scale has been only be observed in peroxide, showing that the LH-MS is not stable and the scission of the O-O bond would be facile. As a result, the formation of LH-MS is exothermic by 0.12 and 0.38 eV with respect to LH-IS1 and LH-TS1, respectively. Further reaction of LH-MS will break the O1-O2 bond to form a physisorbed CO_2 and an O atom adsorbed on CuBSV (LH-FS1). This process requires passing through an energy barrier of 0.11 eV. At the corresponding transition state (LH-TS2), the O1-O2 distance reaches 1.68 Å, the Cu-C distance is enlarged from 2.01 Å in LH-MS to 2.10 Å, while the C-O1 distance is shortened from 1.34 Å to 1.29 Å, implying the strengthening of the C-O1 interaction and the weakening of the O1-O2 and Cu-C interaction have been initiated. Driven by the strong exothermic formation of the C=O bond, the barrier for the formation of physisorbed CO_2 from LH-MS is only 0.11 eV. This suggests that the decomposition of LH-MS is a spontaneous process and is ready to take place at low temperatures. As the E_{ad} of CO_2 is only at the level of -0.01 eV, the desorption of CO_2 in LH-FS1 can also be considered to be barrierless. We then moved on to investigate the reaction between a gaseous CO molecule and the adsorbed O atom over CuBSV (See Fig. 6 and Table 4.).

Table 4. Structural Parameters for Various States along the MEP for the CO Oxidation over CuBSV through LH mechanism.

States	$d_{C\text{-}O}$[a] (Å)	$d_{C\text{-}Cu}$[a] (Å)	$d_{C\text{-}O2}$[a] (Å)	$d_{O2\text{-}Cu}$[a] (Å)	$\angle_{O\text{-}C\text{-}O2}$[b] (°)
LH-IS2	1.15	3.79	2.78	1.75	105.9
LH-TS3	1.15	3.47	2.23	1.78	114.6
LH-FS2	1.17	3.43	1.18	2.65	180.0

[a] Distance between specific atoms. Please see Fig. 6 for the nomination of atoms. [b] Angle among O-C-O2. This angle is 120° in CO_3^{2-} and is 180° in CO_2.

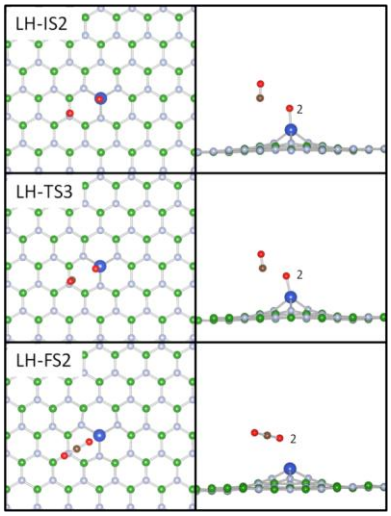

Fig. 6 Top views (left panel) and side views (right panel) of local configurations of the adsorbates on the CuBSV at various states along the minimum-energy pathway via the LH mechanism, including the initial state (LH-IS2), transition state (LH-TS3) and final state (LH-FS2). (B: Green; N: Light blue; Cu: Deep blue; O: Red; C: Brown.)

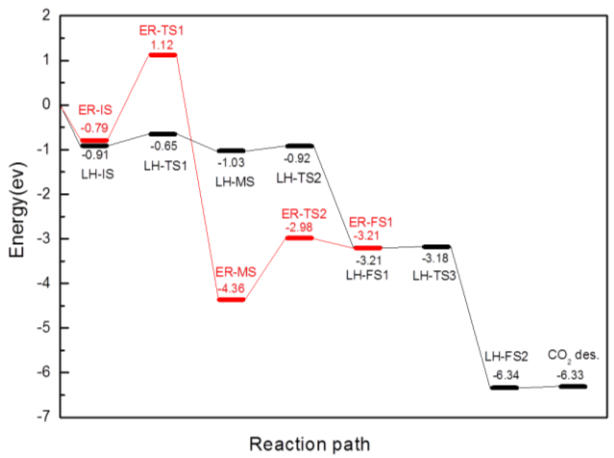

Fig. 7. Schematic energy profile corresponding to local configurations shown in Figures 4, 5 and 6 along the MEP. All energies are given with respect to the reference energy, i.e., the sum of energies of the CuBSV and gaseous CO and O_2 molecules.

A configuration of the CO molecule stands more than 3.0 Å away from the adsorbed atomic O on CuBSV was set as the initial state (LH-IS3, Fig. 6). The product was set to the configuration that CO_2 adsorbed on CuBSV (LH-FS2, Fig. 6). In this process, the C atom of CO approaches to the adsorbed atomic O and pushes it away from the Cu atom to reach LH-TS3. Within LH-TS3, the Cu-C distance is decreased from 3.79 Å in LH-IS2 to 3.47 Å and the C-O2 distance is also decreased from 2.78 to 2.23 Å, showing that due to the formation of interaction between CO and O atom, the CO molecule is pushed to the CuBSV in this endothermic process. As expected from the high reactivity of the adsorbed O atom and the strong exothermic formation of CO_2, the reaction barrier for formation of LH-FS3 is only 0.03 eV and the reaction is exothermic by 3.13 eV with respect to LH-IS2. The low barrier for formation of LH-FS3 and the small E_{ad} of CO_2 indicate that the regeneration of CuBSV as the available reaction center for subsequent CO oxidation is also a spontaneous process even at low temperatures. The thermodynamics profile of the MEP for CO oxidation over CuBSV is summarized in Fig. 7.

To gain more insight into the origin of the high activity of CuBSV, we investigated the electronic structures of selected atomic configurations along the LH reaction path. Fig. 8 shows the DOS of CO and O_2 as well as the Cu-d states in LH-IS1, LH-TS1, LH-MS and LH-TS2, respectively. Due to the minor role of Cu-sp states in CO oxidation, their DOS curves are not shown for clearance. The DOS peaks of Cu-d states, which are crucial for the catalytic activity of CuBSV, are upshifted by the interaction between Cu and *h*-BN and are localized right below the E_F (Fig. 2).

Upon CO and O_2 coadsorption, the peaks of Cu-d states are further shifted to crossing E_F, showing that they are partially occupied in LH-IS1 due to the charge transfer between Cu and adsorbates. The CO-2π* and O_2-2π* states that are of antibonding character, gain electrons and are thus partially filled and downshifted to below the E_F. In addition, the peaks of 5σ states of CO and O_2 are also downshifted to the energy level of the 1π states and get broadened, which is a sign of the contribution of these states to the coadsorption. In this way, the peaks of O_2-5σ, CO-5σ, CO-1π and O_2-1π overlap in the energy range from -7 eV to the E_F, indicating that interaction is already formed between CO and O_2. The peaks of CO-2π* state and the O_2-2π* state also coincide in the range from -1 eV to 1 eV, which implies the interaction between CO and O_2 is weak in LH-IS1.

From LH-IS1 to LH-TS1, the DOS peaks of O_2-1π, O_2-5σ and O_2-2π* states are further downshifted, broadened and overlap with those of CO molecular states which is the result of the evolution of interaction between the coadsorbed molecules. In LH-TS1, as the C-O1 interaction are getting mature, the DOS peaks of O_2 states resonance strongly with those of CO states in the range from -10 eV below E_F to 2 eV above E_F. The peak of O_2 state even overlaps with the CO-4σ state, showing that the C-O interaction in CO is significantly weakened and new C-O1 interaction is formed. These C-O interactions are weak as the resonance between O_2-2π* and CO-2π* of antibonding nature are still strong in the range from -1.5 eV to 1.5 eV. However, the resonance between the CO and O_2 molecular states and Cu-d states of bonding nature is weakened as compared with that in LH-IS1 at about -5 eV, which provides direct evidence for the interaction between Cu and adsorbed molecules, the instability of LH-TS1 and the tendency for peroxide-like intermediate (LH-MS) formation.

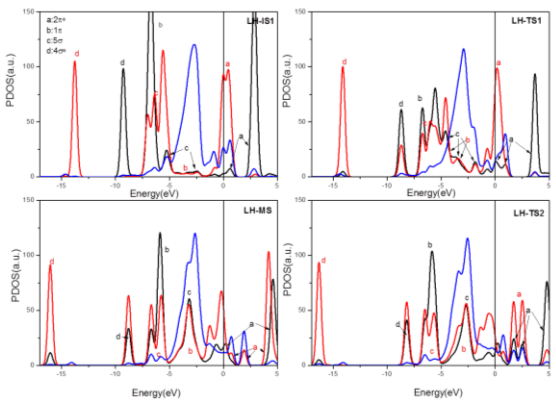

Fig. 8 PDOS of CO,O_2 and Cu atom in the LH-IS1, LH-TS1, LH-MS and LH-TS2. The DOS curves of O2-sp, CO-sp and Cu-d states are in red, black and blue, respectively. The DOS plots were aligned by the calculated E_F. The orbital notations are roughly indicated by a, b, c, and d in reaction processes.

Compared with the DOS plot of LH-TS1, the peaks of adsorbates are narrowed in LH-MS. The DOS peak at -15 eV, originated from the O_2-4σ state is downshifted and overlaps with the CO states, showing that the C-O1 interaction is further strengthened. The intensity of peaks of O_2 states is enhanced in the range from -10 eV to E_F proving that O_2 is activated and C-O1 bonding is stabilized. This is also evidenced by the strong resonance between CO and O_2 states in this energy range. The large broad resonance peak in the range from -7.5 eV to -4.0 eV is split into 2 parts. The part below -5 eV corresponds to the enhanced C-O1 interaction, while the part above -5 eV corresponds to the C-Cu and O2-Cu interactions. These

occupied states are of bonding nature and contribute to the stability of the peroxide-like intermediate on the embedded Cu atom. The reduced intensity of peaks of partial occupied CO and O_2 antibonding states, which are standing on the E_F and resonance with the Cu-d states, shows that this peroxide-like intermediate is ready to dissociate by scission of the O1-O2, C-Cu and O-Cu bonds with the involvement of the Cu-d states.

The DOS peaks of the O_2 and CO states standing at the E_F are split into 2 parts, when the structure evolves from LH-MS to LH-TS2. The part that corresponds to the antibonding interaction between C and O1 is shifted upward and hybrids with the Cu-d states, which is a sign of further enhancement of the C-O1 interaction. The part corresponds to the bonding interaction between C-Cu and O1-Cu is downshifted. This synchronizes the formation and desorption of CO_2 over CuBSV. During the whole process, the Cu-d states hybridize with the molecular states of CO and O_2, proving the significant catalytic role of Cu-d states in coadsorption and subsequent reactions.

In summary, the CO catalytic oxidation over CuBSV is initiated through the LH mechanism, where the coadsorbed CO and O_2 (LH-IS1) react to form a peroxide like complex (LH-MS), by the dissociation of which the a CO_2 molecule and an adsorbed O atom are formed (LH-FS1), and then the CuBSV is regenerated to be available by the reaction of a gaseous CO with the adsorbed O atom (LH-IS2) to form another CO_2 (LH-FS2). The potential high performance of CuBSV can be attributed to the compatibility of the states of CuBSV and adsorbed intermediates, particularly among the Cu-d states and the molecular states of CO and O_2, that facilitates the required charge transfer for the reaction to proceed.

Conclusions

We investigated the electronic structure of Cu atoms embedded in hexagonal boron nitride nanosheet and the mechanisms of CO catalytic oxidation to CO_2 on it by first-principles-based calculations. We showed that Cu atoms prefer to bind directly with the localized defective structures on the boron nitride nanosheet, which act as strong trapping sites for Cu atoms and inhibit their aggregation and clustering. The calculation results indicate that this catalyst is extremely stable and the adsorbed oxygen species can be efficiently activated by the embedded Cu atoms. We investigated and compared the two renowned reaction pathways of the CO oxidation, namely the LH and the ER pathways. We found that the CO oxidation would like to proceed following LH mechanism to produce CO_2 plus an atomic O and then a second CO reacts with the remnant oxygen atom to form CO_2. The calculated energy barriers for formation and dissociation of the peroxide-like intermediate and regeneration of the embedded Cu atoms are as low as 0.26, 0.11 and 0.03 eV, respectively. These energy barriers are already among the lowest reported values, indicating the potential high catalytic performance of Cu atoms embedded in *h*-BN for low temperature oxidation of CO. These findings paved the way for developments of effective CO oxidation catalysts with high stability and superior catalytic performance. It should be noted that one of the outstanding limitations for pratical application of transition metal embedded *h*-BN as catalysts is that a mild and facile route for synthesis of defective *h*-BN hasn't been developed. It is hard to make catalyst-amount TM-embedded *h*-BN with the electron beam radiation. This calls for design and implementation of novel chemical routes that can fabricate defective *h*-BN for trapping of TM atoms or TM-embedded *h*-BN directly.

Acknowledgements

This work was supported by NSFC (21373036, 21103015, 21271037 and 11174045), the Fundamental Research Funds for the Central Universities (DUT12LK14 and DUT14LK09), the Key Laboratory of Coastal Zone Environmental Processes YICCAS (201203), the Key Science and Technology International Co-operation Foundation of Hainan Province, China (KJHZ2014-08) and the Special Academic Partner GCR Program from King Abdullah University of Science and Technology. Y. H would also thank Dalian University of Technology for the Seasky Professorship.

Notes and references

[a] School of Chemistry, Dalian University of Technology, Dalian, 116024, China. Email: xliu@dlut.edu.cn. [b]Advanced Membranes and Porous Materials Center, King Abdullah University of Science and Technology, Thuwal, 23955-6900, Kingdom of Saudi Arabia.

1. A. A. Herzing, C. J. Kiely, A. F. Carley, P. Landon and G. J. Hutchings, *Science*, 2008, **321**, 1331-1335.
2. S. Vajda, M. J. Pellin, J. P. Greeley, C. L. Marshall, L. A. Curtiss, G. A. Ballentine, J. W. Elam, S. Catillon-Mucherie, P. C. Redfern, F. Mehmood and P. Zapol, *Nat. Mater.*, 2009, **8**, 213-216.
3. Y. Lei, F. Mehmood, S. Lee, J. Greeley, B. Lee, S. Seifert, R. E. Winans, J. W. Elam, R. J. Meyer, P. C. Redfern, D. Teschner, R. Schlogl, M. J. Pellin, L. A. Curtiss and S. Vajda, *Science*, 2010, **328**, 224-228.
4. B. T. Qiao, A. Q. Wang, X. F. Yang, L. F. Allard, Z. Jiang, Y. T. Cui, J. Y. Liu, J. Li and T. Zhang, *Nat. Chem.*, 2011, **3**, 634-641.
5. J. Lin, B. T. Qiao, J. Y. Liu, Y. Q. Huang, A. Q. Wang, L. Li, W. S. Zhang, L. F. Allard, X. D. Wang and T. Zhang, *Angew. Chem.-Int. Edit.*, 2012, **51**, 2920-2924.
6. N. Lopez and J. K. Nørskov, *J. Am. Chem. Soc.*, 2002, **124**, 11262-11263.
7. W. T. Wallace and R. L. Whetten, *J. Am. Chem. Soc.*, 2002, **124**, 7499-7505.
8. N. C. Hernández, J. F. Sanz and J. A. Rodriguez, *J. Am. Chem. Soc.*, 2006, **128**, 15600-15601.
9. C. Liu, Y. Tan, S. Lin, H. Li, X. Wu, L. Li, Y. Pei and X. C. Zeng, *J. Am. Chem. Soc.*, 2013, **135**, 2583-2595.
10. M. L. Kimble, A. W. Castleman, R. Mitrić, C. Bürgel and V. Bonačić-Koutecký, *J. Am. Chem. Soc.*, 2004, **126**, 2526-2535.
11. Y. Gao, N. Shao, S. Bulusu and X. C. Zeng, *J. Phys. Chem. C*, 2008, **112**, 8234-8238.
12. R. J. H. Grisel and B. E. Nieuwenhuys, *J. Catal.*, 2001, **199**, 48-59.
13. Z.-P. Liu, P. Hu and A. Alavi, *J. Am. Chem. Soc.*, 2002, **124**, 14770-14779.

14. B. Yoon, H. Hakkinen, U. Landman, A. S. Worz, J. M. Antonietti, S. Abbet, K. Judai and U. Heiz, *Science*, 2005, **307**, 403-407.
15. C.-M. Wang, K.-N. Fan and Z.-P. Liu, *J. Am. Chem. Soc.*, 2007, **129**, 2642-2647.
16. C. Zhang, B. Yoon and U. Landman, *J. Am. Chem. Soc.*, 2007, **129**, 2228-2229.
17. M. F. Camellone and S. Fabris, *J. Am. Chem. Soc.*, 2009, **131**, 10473-10483.
18. M. Haruta, *Catal. Today*, 1997, **36**, 153-166.
19. D. Matthey, J. G. Wang, S. Wendt, J. Matthiesen, R. Schaub, E. Laegsgaard, B. Hammer and F. Besenbacher, *Science*, 2007, **315**, 1692-1696.
20. X. Liu, S. B. Zhang, X. C. Ma, J. F. Jia, Q. K. Xue, X. H. Bao and W. X. Li, *Appl. Phys. Lett.*, 2008, **93**, 093105.
21. B. Hammer and J. K. Norskov, in *Advances in Catalysis*, Academic Press Inc, San Diego, 2000, pp. 71-129.
22. I. N. Remediakis, N. Lopez and J. K. Norskov, *Angew. Chem.-Int. Edit.*, 2005, **44**, 1824-1826.
23. L. Li, A. H. Larsen, N. A. Romero, V. A. Morozov, C. Glinsvad, F. Abild-Pedersen, J. Greeley, K. W. Jacobsen and J. K. Norskov, *J. Phys. Chem. Lett.*, 2013, **4**, 222-226.
24. M. S. Chen and D. W. Goodman, *Chem. Soc. Rev.*, 2008, **37**, 1860-1870.
25. M. S. Chen and D. W. Goodman, *Science*, 2004, **306**, 252-255.
26. Y. X. Yao, X. Liu, Q. Fu, W. X. Li, D. L. Tan and X. H. Bao, *ChemPhysChem*, 2008, **9**, 975-979.
27. M. Bowker, *Nat. Mater.*, 2002, **1**, 205-206.
28. J. Zhang, X. Liu, M. N. Hedhili, Y. Zhu and Y. Han, *ChemCatChem*, 2011, **3**, 1294-1298.
29. A. Uzun, V. Ortalan, Y. L. Hao, N. D. Browning and B. C. Gates, *ACS Nano*, 2009, **3**, 3691-3695.
30. A. Uzun, V. Ortalan, N. D. Browning and B. C. Gates, *J. Catal.*, 2010, **269**, 318-328.
31. X. Zhang, H. Shi and B. Q. Xu, *Angew. Chem.-Int. Edit.*, 2005, **44**, 7132-7135.
32. A. V. Krasheninnikov, P. O. Lehtinen, A. S. Foster, P. Pyykko and R. M. Nieminen, *Phys. Rev. Lett.*, 2009, **102**, 126807.
33. X. Liu, C. G. Meng and Y. Han, *J. Phys. Chem. C*, 2013, **117**, 1350-1357.
34. X. Liu, C. G. Meng and Y. Han, *Nanoscale*, 2012, **4**, 2288-2295.
35. X. Liu, L. Li, C. G. Meng and Y. Han, *J. Phys. Chem. C*, 2012, **116**, 2710-2719.
36. K. X. Yao, X. Liu, Z. Li, C. C. Li, H. C. Zeng and Y. Han, *ChemCatChem*, 2012, **4**, 1938-1942.
37. X. Liu, C. Meng and Y. Han, *Phys. Chem. Chem. Phys.*, 2012, **14**, 15036-15045.
38. X. Liu, Y. Sui, C. Meng and Y. Han, *RSC Adv.*, 2014, **4**, 22230-22240.
39. X. Liu, K. X. Yao, C. Meng and Y. Han, *Dalton Trans.*, 2012, **41**, 1289-1296.
40. H. Wang, Q. Wang, Y. Cheng, K. Li, Y. Yao, Q. Zhang, C. Dong, P. Wang, U. Schwingenschlögl, W. Yang and X. X. Zhang, *Nano Lett.*, 2011, **12**, 141-144.
41. Y. H. Lu, M. Zhou, C. Zhang and Y. P. Feng, *J. Phys. Chem. C*, 2009, **113**, 20156-20160.
42. F. Li, J. Zhao and Z. Chen, *J. Phys. Chem. C*, 2011, **116**, 2507–2514.
43. Y. Li, Z. Zhou, G. Yu, W. Chen and Z. Chen, *J. Phys. Chem. C*, 2010, **114**, 6250-6254.
44. E. H. Song, Z. Wen and Q. Jiang, *J. Phys. Chem. C*, 2011, **115**, 3678-3683.
45. X. Liu, Y. Sui, T. Duan, C. Meng and Y. Han, *Phys. Chem. Chem. Phys.*, 2014, DOI: 10.1039/C1034CP02106A.
46. M. Corso, W. Auwarter, M. Muntwiler, A. Tamai, T. Greber and J. Osterwalder, *Science*, 2004, **303**, 217-220.
47. A. B. Preobrajenski, M. A. Nesterov, M. L. Ng, A. S. Vinogradov and N. Martensson, *Chem. Phys. Lett.*, 2007, **446**, 119-123.
48. W. Q. Han, L. J. Wu, Y. M. Zhu, K. Watanabe and T. Taniguchi, *Appl. Phys. Lett.*, 2008, **93**, 223103.
49. A. Nag, K. Raidongia, K. Hembram, R. Datta, U. V. Waghmare and C. N. R. Rao, *ACS Nano*, 2010, **4**, 1539-1544.
50. C. Y. Zhi, Y. Bando, C. C. Tang, H. Kuwahara and D. Golberg, *Adv. Mater.*, 2009, **21**, 2889-2893.
51. K. Watanabe, T. Taniguchi and H. Kanda, *Nat. Mater.*, 2004, **3**, 404-409.
52. A. Zobelli, C. P. Ewels, A. Gloter, G. Seifert, O. Stephan, S. Csillag and C. Colliex, *Nano Lett.*, 2006, **6**, 1955-1960.
53. J. C. Meyer, A. Chuvilin, G. Algara-Siller, J. Biskupek and U. Kaiser, *Nano Lett.*, 2009, **9**, 2683-2689.
54. C. H. Jin, F. Lin, K. Suenaga and S. Iijima, *Phys. Rev. Lett.*, 2009, **102**, 195505.
55. A. J. Du, Y. Chen, Z. H. Zhu, R. Amal, G. Q. Lu and S. C. Smith, *J. Am. Chem. Soc.*, 2009, **131**, 17354-17359.
56. S. Lin, X. Ye, R. S. Johnson and H. Guo, *J. Phys. Chem. C*, 2013, **117**, 17319–17326.
57. P. Zhao, Y. Su, Y. Zhang, S.-J. Li and G. Chen, *Chem. Phys. Lett.*, 2011, **515**, 159-162.
58. C. J. Huang, X. X. Ye, C. Chen, S. Lin and D. Q. Xie, *Comput. Theor. Chem.*, 2013, **1011**, 5-10.
59. M. Gao, A. Lyalin and T. Taketsugu, *J. Chem. Phys.*, 2013, **138**, 034701.
60. B. Delley, *J. Chem. Phys.*, 1990, **92**, 508-517.
61. B. Delley, *J. Chem. Phys.*, 2000, **113**, 7756-7764.
62. J. P. Perdew, K. Burke and M. Ernzerhof, *Phys. Rev. Lett.*, 1996, **77**, 3865-3868.
63. B. Delley, *Phys. Rev. B*, 2002, **66**, 155125.
64. X. Liu, C. G. Meng and C. H. Liu, *Phase Transit.*, 2006, **79**, 249-259.
65. X. Liu, C. G. Meng and C. H. Liu, *Acta Phys.-Chim. Sin.*, 2004, **20**, 280-284.
66. V. A. Finkel, G. P. Kovtun and M. I. Palatnik, *Phys. of Metals and Metallography (USSR)*, 1971, **32**, 231-235.
67. A. H. Castro Neto, F. Guinea, N. M. R. Peres, K. S. Novoselov and A. K. Geim, *Rev Mod Phys*, 2009, **81**, 109-162.
68. H. J. Monkhorst and J. D. Pack, *Phys. Rev. B*, 1976, **13**, 5188-5192.
69. F. L. Hirshfeld, *Theor. Chim. Acta*, 1977, **44**, 129-138.
70. N. Govind, M. Petersen, G. Fitzgerald, D. King-Smith and J. Andzelm, *Comput. Mater. Sci.*, 2003, **28**, 250-258.
71. M. Gao, A. Lyalin and T. Taketsugu, *J. Phys. Chem. C*, 2012, **116**, 9054-9062.
72. J. H. Kwak, J. Z. Hu, D. Mei, C. W. Yi, D. H. Kim, C. H. F. Peden, L. F. Allard and J. Szanyi, *Science*, 2009, **325**, 1670-1673.

73. S. Sun, G. Zhang, N. Gauquelin, N. Chen, J. Zhou, S. Yang, W. Chen, X. Meng, D. Geng, M. N. Banis, R. Li, S. Ye, S. Knights, G. A. Botton, T.-K. Sham and X. Sun, *Sci. Rep.*, 2013, **3**, 1775.
74. Z. L. Liu, Q. Z. Xue, T. Zhang, Y. H. Tao, C. C. Ling and M. X. Shan, *J. Phys. Chem. C*, 2013, **117**, 9332-9339.
75. M. Gajdos, A. Eichler and J. Hafner, *J. Phys.-Condes. Matter*, 2004, **16**, 1141-1164.
76. W. X. Li, C. Stampfl and M. Scheffler, *Phys. Rev. B*, 2002, **65**, 075407.
77. X. Liu, H. Guo and C. Meng, *J. Phys. Chem. C*, 2012, **116**, 21771-21779.
78. Y. Zhao, X. Liu, K. X. Yao, L. Zhao and Y. Han, *Chem. Mat.*, 2012, **24**, 4725-4734.
79. G. Kim and S.-H. Jhi, *ACS Nano*, 2011, **5**, 805-810.
80. K. J. Laidler, *Pure Appl. Chem.*, 1996, **68**, 149-192.